

Quantification of Biological Interactions with Particle Image Cross-Correlation Spectroscopy (PICCS)

Stefan Semrau,^{†△} Laurent Holtzer,^{†△} Marcos González-Gaitán,[‡] and Thomas Schmidt^{†*}

[†]Physics of Life Processes, Leiden Institute of Physics, Leiden University, Leiden, The Netherlands; and [‡]Department of Biochemistry, University of Geneva, Geneva, Switzerland

ABSTRACT A multitude of biological processes that involve multiple interaction partners are observed by two-color microscopy. Here we describe an analysis method for the robust quantification of correlation between signals in different color channels: particle image cross-correlation spectroscopy (PICCS). The method, which exploits the superior positional accuracy obtained in single-object and single-molecule microscopy, can extract the correlation fraction and length scale. We applied PICCS to correlation measurements in living tissues. The morphogen Decapentaplegic (Dpp) was imaged in wing imaginal disks of fruit fly larvae and we quantified what fraction of early endosomes contained Dpp.

INTRODUCTION

In the past, several techniques have been developed for the quantification of spatial correlation between two fluorescently labeled interaction partners. In particular, single-molecule fluorescence assays have been used successfully to measure colocalization (1–3). Single-molecule fluorescence techniques require only small amounts of fluorescent labels and contain information about positional correlations on subdiffraction length scales (4). However, the direct mapping between single-molecule signals from two different channels is prone to a systematic error: colocalization is typically defined by a distance threshold below which two signals are considered colocalized. Therefore, a priori knowledge about the distribution of distances, about the positional error, and about the experimentally unavoidable alignment mismatch between two detection channels is needed to find a proper threshold. Even without any real correlation, this method will always yield colocalization events due to accidental proximity of signals. This problem aggravates with increasing signal density. Hence, even with the highest spatial resolution, proximity is not the optimal readout for correlation.

Fluorescence cross-correlation spectroscopy and image cross-correlation spectroscopy (ICCS) directly determine the cross-correlation between the two different color channels (5,6) without the need for a threshold. However, fluorescence cross-correlation spectroscopy is restricted to fast moving molecules and does not contain spatial information. ICCS on the other hand produces quantitative results for the correlation fraction but a nonuniform distribution of molecules can bias the results. Image scrambling strategies can relieve this problem (7), but they limit the length scale on which correlations can be detected. ICCS also requires

a certain minimal fluorescence signal which excludes, for example, the study of receptors which are present in low copy numbers only.

Two further, recently developed, techniques, which address the correlation of two molecular species are cross-correlation raster imaging correlation spectroscopy (8) and the two-color number and brightness analysis (9). Although these techniques are readily applicable on commercially available microscopes and provide information about the spatial distribution of correlated species they are sensitive to microscope settings and fail to produce absolute numbers for the correlation fraction. Apart from single-molecule tracking, all above-mentioned techniques are diffraction-limited, and therefore cannot measure the molecular correlation length.

Here we show how the advantages of ICCS and single-particle tracking can be combined in one analysis technique: particle image cross-correlation spectroscopy (PICCS). This technique is largely based on particle image correlation spectroscopy (PICS) developed by us before (4). PICCS uses high accuracy single-molecule/single-object position data, but instead of correlating the positions of the same molecular species at several points in time (as is done in PICS), PICCS correlates the positions of two molecular species at the same point in time in two separate channels adopting the approach employed by ICCS (6).

In what follows, we first provide a theoretical description of PICCS, after which we validate the method using fluorescent beads. One particular example for biological interactions which can be studied with the help of PICCS is the trafficking of the morphogen Decapentaplegic (Dpp) through endosomes. Dpp forms a gradient in the developing wing imaginal disk of the fruit fly *Drosophila melanogaster*, ultimately controlling patterning and growth of the tissue. Dpp originates from a stripe of Dpp-producing cells at the anterior-posterior compartment boundary (10), and is secreted to neighboring cells. With PICCS we determined

Submitted July 27, 2010, and accepted for publication December 23, 2010.

[△]Stefan Semrau and Laurent Holtzer contributed equally to this work.

*Correspondence: schmidt@physics.leidenuniv.nl

Editor: David E. Wolf.

© 2011 by the Biophysical Society
0006-3495/11/04/1810/9 \$2.00

doi: 10.1016/j.bpj.2010.12.3746

which fraction of early endosomes contained Dpp and vice versa.

THEORY

Particle image cross-correlation spectroscopy (PICCS) is a method to quantitatively determine the correlation between two interaction partners labeled with two spectrally distinguishable fluorophores. The interaction partners can be single molecules or extended objects. We assume that their density is so low that they can be resolved individually and their position determined with a high positional accuracy (11–13). For simplicity, we will denote the signals coming from the two fluorophores by “YFP” and “CFP” without loss of generality. The task at hand is to determine the correlation fraction of the interaction partners, i.e., to determine the fraction of CFP signals which are correlated with YFP signals (or vice versa).

The PICCS algorithm

The first step in the PICCS analysis is identical to existing single-molecule tracking methods (2,3): the position of YFP and CFP signals is determined with subdiffraction positional accuracy, for example by fitting two-dimensional Gaussians to the fluorescence signals. Subsequently a cross-correlation function $C_{cum}(l)$ between the two channels is calculated with an ensemble approach. $C_{cum}(l)$ is equal to the average number of CFP signals at time $t + \Delta t$ which have a distance smaller than l to a certain YFP signal at time t (Fig. 1). When both fluorophores are imaged at the same time, $\Delta t = 0$ s. To avoid edge effects, only those YFP signals are used which lie farther away from the edges of the image than a predefined maximal distance l_{max} ($0 < l < l_{max}$, see dashed line in Fig. 1).

As detailed below, this procedure results in a correlation function of the form

$$C_{cum}(l) = \alpha P_{cum}(l) + c_{CFP} \cdot \pi l^2, \quad (1)$$

if the uncorrelated CFP signals are distributed randomly with a uniform density c_{CFP} . $P_{cum}(l)$ is the cumulative probability to find a distance smaller than l between a YFP and a CFP signal, which are correlated. Here, α is the correlation fraction, i.e., the fraction of YFP signals which are correlated with a CFP signal. The value $\alpha = 1$ if there is a corresponding CFP signal for any YFP signal and $\alpha = 0$ if CFP and YFP signals are completely uncorrelated. An example for $C_{cum}(l)$ calculated from simulated data is given in Fig. 2.

The cumulative correlation function

To derive the expression for $C_{cum}(l)$ given in Eq. 1 we start from the probability $P(x,y)$ to find two correlated signals separated by a vector (x,y) . The cumulative probability $P_{cum}(l)$ is found by integration of $P(x,y)$ in polar coordinates

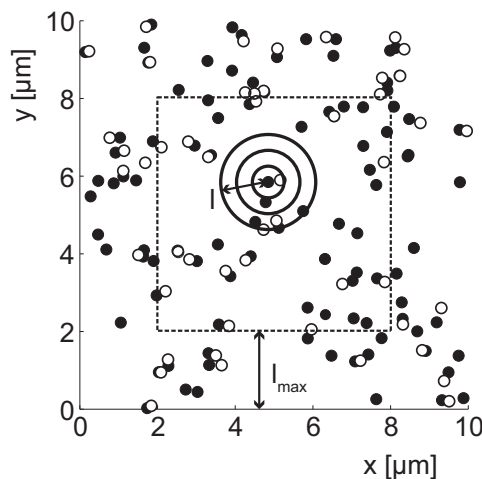


FIGURE 1 PICCS algorithm. For all YFP signals (solid circles) the number of CFP signals (open circles) is counted which fall into a circle of radius l from a YFP signal. The total number is subsequently divided by the number of YFP signals. By increasing l from 0 to l_{max} the correlation function $C_{cum}(l)$ is constructed. (Dashed line) Area in which the YFP signals are used for analysis. This area is separated from the edges of the image by l_{max} (in this figure $l_{max} = 2 \mu\text{m}$ is taken). The signal positions were simulated with the following parameters: density of YFP signals $c_{YFP} = 1 \mu\text{m}^{-2}$, correlation fraction $\alpha = 0.5$ (results in a density of CFP signals of $c_{CFP} = 0.5 \mu\text{m}^{-2}$), and correlation length $\sigma = 150$ nm.

$$P_{cum}(l) = \int_0^l dr r \int_0^{2\pi} d\phi P(r, \phi), \quad (2)$$

$$r = \sqrt{x^2 + y^2},$$

$$\phi = \arctan(y/x).$$

The shape of the function $P_{cum}(l)$ depends on the nature of the interaction between the interaction partners and the positional accuracy for determination of the YFP and CFP signals. The experimentally observed $P(x,y)$ is found from the convolution of the real correlation $P_{corr}(x,y)$, which is characteristic for a specific interaction, and the probability

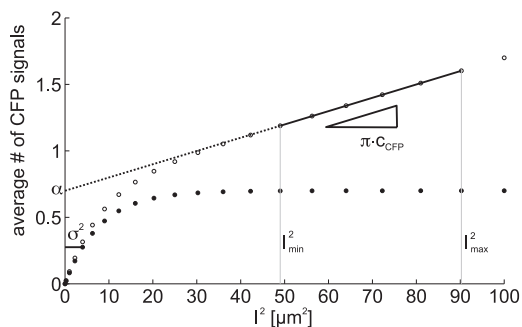


FIGURE 2 The cumulative correlation function. (Open circles) $C_{cum}(l)$ calculated from simulated data. (Solid circles) $C_{cum}(l)$ after subtraction of the linear contribution (dotted line). To determine the slope $\pi \cdot c_{CFP}$ of the linear contribution, a straight line is fitted to $C_{cum}(l)$ between l_{min} and l_{max} . The offset of this straight line is equal to the correlation fraction α . The value σ is equal to the distance l where the function $C_{cum}(l) - \pi \cdot c_{CFP} l^2$ has the value $\alpha(1 - \sqrt{e})$.

density $P_{pos. acc.}(x,y)$ describing the (apparent) correlation due to the finite positional accuracy (14),

$$P(x,y) = \int \int dx' dy' P_{corr}(x-x', y-y') P_{pos. acc.}(x', y') \quad (3)$$

$$P_{pos. acc.}(x,y) = \frac{1}{2\pi\sigma^2} \exp\left(-\frac{x^2+y^2}{2\sigma^2}\right)$$

where $\sigma = \sqrt{2}\delta$ and δ is the one-dimensional positional accuracy.

In the simplest case, if the YFP and CFP signal are at the same position, $P_{cum}(l)$ is determined by the positional accuracy alone:

$$P_{cum}(l) = 1 - \exp\left(-\frac{l^2}{2\sigma^2}\right). \quad (4)$$

A fit of Eq. 4 to $P_{cum}(l)$ with σ as the free fit parameter results in a value for the one-dimensional positional accuracy $\delta = \sigma/\sqrt{2}$. More generally, σ can be regarded as a typical correlation length.

To accurately describe the experimentally determined $P_{cum}(l)$ we found that we had to assume two correlation lengths (σ_1 and σ_2) (see Experimental Validation),

$$P_{cum}(l) = \beta \left(1 - \exp\left(-\frac{l^2}{2\sigma_1^2}\right)\right) + (1 - \beta) \left(1 - \exp\left(-\frac{l^2}{2\sigma_2^2}\right)\right), \quad (5)$$

where β is the fraction of data that has a correlation length σ_1 . We suppose that a broad distribution of positional accuracies explains this functional form of $P_{cum}(l)$.

If, per image, there is only one pair of correlated signals the correlation function $C_{cum}(l)$ equals $P_{cum}(l)$: $C_{cum}(l) = P_{cum}(l)$. If only for a fraction α of all YFP signals there is a correlated CFP signal, we observe $C_{cum}(l) = \alpha P_{cum}(l)$. Typically, there is more than one YFP signal per image and therefore also more than one CFP signal. If l gets bigger, neighboring CFP signals in close proximity are counted by the PICCS algorithm although they are not correlated with the YFP signal. Additionally there might be CFP signals which are not correlated with any YFP signal. These CFP signals, in close proximity or not correlated with any YFP signal, lead to an additional contribution $c_{CFP} \cdot \pi l^2$ to $C_{cum}(l)$. Here we assume that the positions of the CFP signals follow a uniform random distribution with density c_{CFP} . In total, $C_{cum}(l) = \alpha P_{cum}(l) + c_{CFP} \cdot \pi l^2$.

If there are no CFP signals in addition to the ones correlated with a YFP one, c_{CFP} can be calculated from the density of YFP signals c_{YFP} , the correlation fraction α , and the image area A by

$$c_{CFP} = \alpha(c_{YFP}A - 1)/A = \alpha(c_{YFP} - 1/A) \equiv c_{CFP}^*. \quad (6)$$

If $\alpha/A \ll c_{YFP}$, $c_{CFP} \approx \alpha c_{YFP}$. In general, $c_{CFP} = c_{YFP}^* + c_{CFP, uncorr.}$, where $c_{CFP, uncorr.}$ is the density of CFP signals which are not correlated with any YFP signal.

Inhomogeneous, nonrandom distribution of signals

In the form presented so far, the algorithm requires a random, homogeneous distribution of CFP signals, which results in the term $c_{CFP} \cdot \pi l^2$ in Eq. 1. In a real-life situation, the assumption that all CFP signals are distributed randomly with a uniform density might be violated. One reason is the diffraction limit: if two molecules are too close to each other (<200 nm), their fluorescence signals will merge and only one signal is observed. Consequently, close to a given CFP signal the probability to find another signal is decreased. Additionally, there might be biological reasons for correlations between the CFP signals. For example, receptors might be distributed evenly (and nonrandomly) to achieve optimal surface coverage. To correct for an inhomogeneous or nonrandom distribution of CFP signals we can calculate the spatial correlation among CFP signals by regular PICS (see Semrau and Schmidt (4)). Any correlation between the positions of CFP signals will cause a deviation from the simple quadratic contribution $c_{CFP} \cdot \pi l^2$, we assumed. The influence of this correlation on the cumulative correlation $C_{cum}(l)$ between the two color channels depends on the distribution of distances between YFP and CFP signals $P_{cum}(l)$. We define the function $s(r,l)$ as the number of CFP signals in a circle with radius l if the distance between the YFP signal and a correlated CFP signal is r . For YFP signals which have a correlated CFP signal, the contribution of uncorrelated signals can be written as

$$\alpha \int_0^\infty dr s(r,l) \frac{\partial P_{cum}(r)}{\partial r}, \quad (7)$$

where $\partial P_{cum}(r)/\partial r$ gives the probability for a distance r between a pair of correlated signals. For YFP signals without correlated CFP signals, we keep the simple quadratic dependence and arrive at

$$C_{cum}(l) = \alpha P_{cum}(l) + (1 - \alpha) c_{CFP} \cdot \pi l^2 + \alpha \int_0^\infty dr s(r,l) \frac{\partial P_{cum}(r)}{\partial r}, \quad (8)$$

where $s(r,l)$ is determined empirically from the experimental data by correlation of a virtual YFP channel image with the measured images from the CFP channel. The virtual YFP image is constructed from the CFP image by placing YFP signals at a distance r from a CFP signal. The $C_{cum}(l)$ determined for a given r with the standard algorithm is equal to $s(r,l)$. Typically, the results from 20 virtual images (where the YFP signals are positioned equally spaced on circles with radius r around the CFP signals) are averaged to obtain $s(r,l)$.

Subsequent to the calculation of $s(r,l)$, the correction is determined numerically by the following self-consistent algorithm:

Step 1. As an initial guess for the correction term, determine the slope of the linear part of C_{cum} and use the original correction term from Eq. 1;

- Step 2. Subtract the correction;
- Step 3. Determine α as the average over the flat part of the resulting curve;
- Step 4. Normalize to 1 and fit the model Eq. 5;
- Step 5. Calculate the new correction according to Eq. 8, then go to Step 2.

Steps 2–5 are repeated until the fit parameters change less than a predefined threshold.

To validate this algorithm we have conducted simulations in which two highly inhomogeneous situations were considered. First, we simulated a system with highly clustered signals and secondly, signals on a distorted square lattice (anti-correlated signals) were considered. The details and results of these simulations are described in the [Supporting Material](#).

MATERIALS AND METHODS

Imaging of fruit fly wing disks

The *UAS-YFP-Dpp* line was generated by using the existing *UAS-GFP-Dpp* vector (15) where GFP was replaced by YFP (Venus) (16). The *dpp^{Δ8}/dpp^{Δ12}*; *dpp-Gal4/UAS-YFP-Dpp* flies have an identical wing phenotype to the *dpp^{Δ8}/dpp^{Δ12}*; *dpp-Gal4/UAS-GFP-Dpp* flies (15): they survive to adulthood and have normally patterned wings, although smaller in size (data not shown). For detection of early endosomes in wing imaginal disks, we used the following genotype: *tub-CFP-Rab5* (17). Previously we have shown that Rab5-endosomes accumulate cargo upon a short or long chase, respectively, in pulse/chase experiments (15). Expression of CFP-Rab5 is moderate and no effects on the size or amount of early endosomes was observed (17). Furthermore, experiments in A431 cells showed that a five-fold overexpression of GFP-Rab5 compared to endogenous Rab5 did not significantly change the population of early endosomes (18).

To obtain wing imaginal disks, third instar larvae (*tubulin-Rab5-CFP*; *dpp-Gal4/UAS-YFP-Dpp*) were dissected in Clone8 medium (Shields & Sang M3 Medium containing 2% Fetal Calf Serum, 2.5% Fly Extract, 12.5 IU Insulin/100 mL medium, and 1× Penicillin/Streptomycin; Sigma-Aldrich, St. Louis, MO), after which the wing imaginal disks were mounted in a custom-made sample holder. Nail polish was used for sealing of the sample holder. The wing imaginal disks were imaged ~10 min after dissection. Samples were discarded 1 h after dissection.

Imaging was done on a three-dimensional, wide-field fluorescence microscope as previously described in Holtzer et al. (19). To image a z range of ~4 μm , image stacks were generated using a piezo-driven objective holder (Physik Instrumente, Karlsruhe, Germany) to move the objective in axial direction. Each image stack contained five image planes with $\Delta z = 0.7 \mu\text{m}$ between each image plane. The time between image planes was 40 ms, during which the movement of the endosomes was negligible. Therefore, each image stack was assumed to be acquired at one time point. Wing imaginal disk samples were excited by an Argon-ion laser (Coherent Laser, Santa Clara, CA) at either 458 nm to excite Rab5-CFP or 514 nm to excite Dpp-YFP.

An alternating excitation pattern was used to distinguish between the two fluorophores. The pattern consisted of one image stack which was excited at 458 nm and consecutively 10 image stacks were excited at 514 nm with a stack rate of 1 Hz. The fast switching between laser lines was done using an Acousto-Optic Tunable Filter (AA Opto-Electronic, Orsay, France). This pattern was chosen to minimize photobleaching of the CFP, as the amount of Rab5-CFP per endosome was lower than the amount of Dpp-YFP. Imaging was done in the apical region of the cells because most of the endosomes are located there (20). Dpp-producing cells (the source) were located by eye using a Mercury lamp (Zeiss, Oberkochen, Germany) for excitation.

Using a motorized stage the center of the image was typically 20 μm displaced from the source, with an image area of 100 μm^2 showing ~17 cells in each experiment. The position of endosomes was detected as described before (12,19).

Imaging of fluorescent beads

To experimentally validate the PICCS-method 20-nm yellow-green Fluospheres and 200-nm Tetraspek microspheres (both Molecular Probes, Leiden, The Netherlands) were used. Beads were mixed at different ratios (including samples containing only yellow-green beads or tetraspek beads) and spin-coated onto a glass coverslip. Imaging was done using alternating laser excitation using an Argon-ion laser (Coherent Laser) at 488 nm to excite both yellow-green beads and tetraspek beads and a 639-nm diode laser (Power Technology, Alexander, AR) to excite only tetraspek beads. Movies were taken at random positions on the coverslip (image size 25 × 25 μm). For the samples with mixed beads, the number of positions was 30 giving a total number of beads $n > 200$ for each mixing ratio.

RESULTS

Error scaling simulation

To design a successful experiment it is crucial to know how the error of the measured observables (α , c_{CFP} , and σ) scales with the experimental and fitting parameters (Fig. 2). We determined the error by application of the PICCS algorithm described above to simulated data, assuming that the signals are distributed randomly and uniformly in space and the correlations are governed by Eq. 1. First, we assumed that all CFP signals are correlated with a YFP signal, so $c_{CFP} = \alpha(c_{YFP} - 1/A)$, where A is the area of the image. Then we added additional CFP signals, which are not correlated with any YFP signal. For every set of parameters, the simulations were repeated 100 times and the errors $\Delta\alpha$, Δc_{CFP} , and $\Delta\sigma$ were determined as the standard deviation.

Experimental parameters

The experimental parameters are the correlation fraction α , the density of YFP and CFP signals c_{YFP} and c_{CFP} , the correlation length σ , and the number of images M . As evident from Fig. 3 a, all errors scaled approximately like $1/\sqrt{M}$ where M is the number of acquired images. This behavior assures that any error can be made small just by acquisition of more images. The same scaling behavior was found for α , see Fig. 3 b. As to be expected, the relative errors became large when the correlation fraction was small or, equivalently, more images would have to be acquired to achieve a certain accuracy. The dependence of the error on the density of YFP signals c_{YFP} was different for the various observables (Fig. 3 c). While the error for c_{CFP} scaled like the inverse square-root ($1/\sqrt{c_{YFP}}$), the errors of α and σ were fitted with the empirical model

$$A \cdot (c_{YFP}/\mu\text{m}^{-2})^{-0.5} + B \cdot (c_{YFP}/\mu\text{m}^{-2})^{0.25}.$$

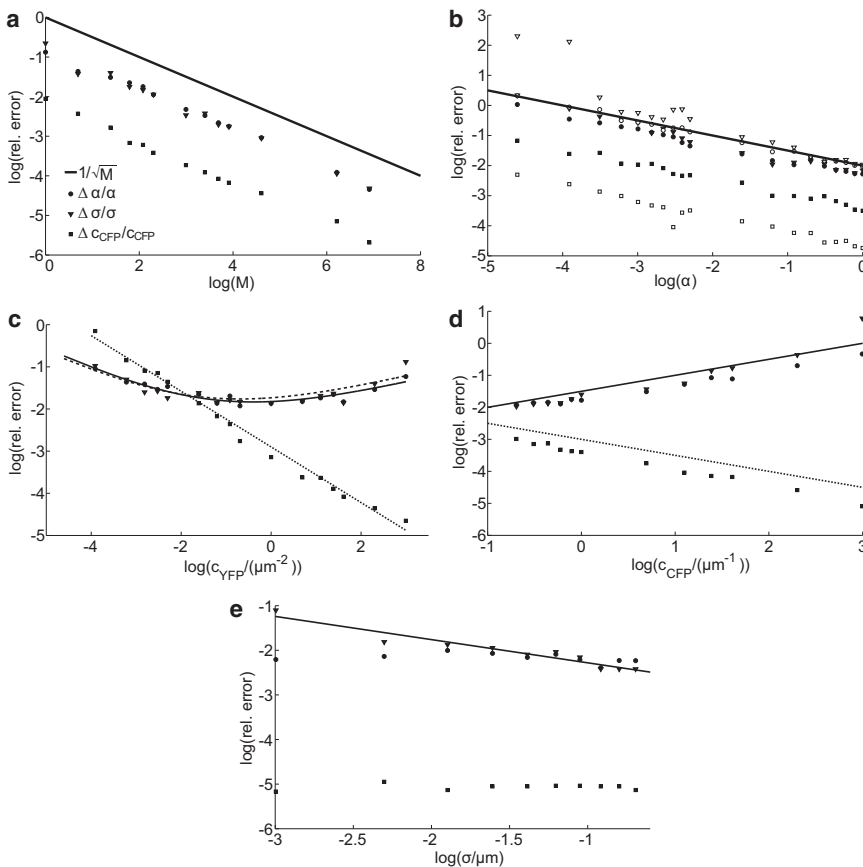


FIGURE 3 Dependence of the relative errors on the number of images M . (a) The relative errors of α (circles), σ (triangles), and c_{CFP} (squares) all scaled approximately like $1/\sqrt{M}$ (solid line). $M = 10$, $\alpha = 0.5$, $c_{YFP} = 0.5 \mu\text{m}^{-2}$, and $\sigma = 0.15 \mu\text{m}$. (b) Dependence of the relative errors on the interaction fraction α . The legend is the same as in panel a, where $c_{YFP} = 1 \mu\text{m}^{-2}$ (solid symbols), $c_{YFP} = 10 \mu\text{m}^{-2}$ (open symbols), $M = 10$, and $\sigma = 0.15 \mu\text{m}$ in both cases. The errors of all determined parameters approximately scaled like $1/\sqrt{\alpha}$ (solid line), independent of the density c_{YFP} . (c) Dependence of the relative errors on the density c_{YFP} . The legend is the same as in panel a. The relative error of α (circles) and σ (triangles) were fitted with the model $A \cdot (c_{YFP}/\mu\text{m}^{-2})^{-0.5} + B \cdot (c_{YFP}/\mu\text{m}^{-2})^{0.25}$ (solid and dashed line, respectively). For $\alpha A = 0.04$, $B = 0.12$, which resulted in a minimum at $0.6 \mu\text{m}^{-2}$ and for $\sigma A = 0.07$, $B = 0.14$, which gave a minimum at $0.5 \mu\text{m}^{-2}$. The relative error of c_{CFP} (squares) scaled approximately like $c_{YFP}^{-2/3}$. (Shaded line) Linear fit in the logarithmic plot given by $y = -0.66(c_{CFP}/\mu\text{m}^{-1}) - 2.9$. $M = 10$, $\alpha = 0.5$, and $\sigma = 0.15 \mu\text{m}$. (d) Dependence of the relative errors on the density c_{CFP} . The legend is the same as in panel a. The relative error of α and σ scaled approximately like $\sqrt{c_{CFP}}$ (solid line), the relative error of c_{CFP} scaled like $1/\sqrt{c_{CFP}}$ (dashed line). $M = 10$, $c_{YFP} = 1 \mu\text{m}^{-2}$, $\alpha = 0.5$, and $\sigma = 0.15 \mu\text{m}$. (e) Dependence of the relative errors on σ . The legend is the same as in panel a. The relative error of α and c_{CFP} did not change significantly with σ . The relative error of σ scaled approximately like $1/\sqrt{\sigma}$ (solid line) is a linear fit in the logarithmic plot given by $y = -0.52(c_{YFP}/\mu\text{m}^{-2}) - 2.8$. $M = 50$, $c_{YFP} = 1 \mu\text{m}^{-2}$, and $\alpha = 0.5$.

This model has a minimum at $(2A/B)^{4/3}$, which implies that there is an optimal density c_{YFP} , where the errors are minimal. As will become clear below, the value of this optimal density depends on the fitting parameters. The errors of α and σ initially decreased with increasing c_{YFP} because of the higher number of YFP signals, which increased statistical significance. At the same time, c_{CFP} increased and therefore the contribution $c_{CFP} \cdot \pi l^2$ increased relative to α . Consequently, the errors of α and σ increased for big densities c_{YFP} .

So far, all CFP signals had a corresponding (i.e., correlated) YFP signal. Next, we added additional, noncorrelated CFP signals. If the density of YFP signals c_{YFP} and the interaction fraction α were kept constant, α and σ scaled approximately like $\sqrt{c_{CFP}}$ while the error of c_{CFP} scaled like $1/\sqrt{c_{CFP}}$ (Fig. 3 d). As to be expected, the presence of extra CFP signals made the determination of α and σ increasingly difficult. A change in the correlation length σ had significant influence only on the error for σ which scaled like $1/\sqrt{\sigma}$. For increasing σ , there were more data points in a region which is important for the determination of σ , namely where $P_{cum}(l)$ is significantly smaller than 1. The errors of α and c_{CFP} were approximately constant (Fig. 3 e).

Fitting parameters

The fitting parameters are the length of the interval for the linear fit $l_{max} - l_{min}$, its center $l_{center} = (l_{max} - l_{min})/2$ and the distance between two data points Δl (Fig. 2). Fig. 4, a–c, shows that the general scaling behavior was independent on the position of the fit interval l_{center} . However, the position of the minimum error of α and σ depended on l_{center} : The bigger l_{center} , the smaller the optimal density c_{YFP} . Therefore, l_{center} should be as small as the data allows—of course, the fit interval must be in the region where $C_{cum}(l)$ is linear when plotted versus l^2 . Fig. 4, d and e, shows the dependence on the errors on the length of the fit interval and the distance between data points, respectively. The errors asymptotically became constant for big fit intervals and small distances between data points. Note that increasing l_{max} at constant l_{min} enlarged the fit interval but also moved its center l_{center} , which is disadvantageous, see above.

Experimental validation

Fluorescent beads

To verify that PICCS retrieves the true correlation fractions we performed experiments with known ratios of two kinds

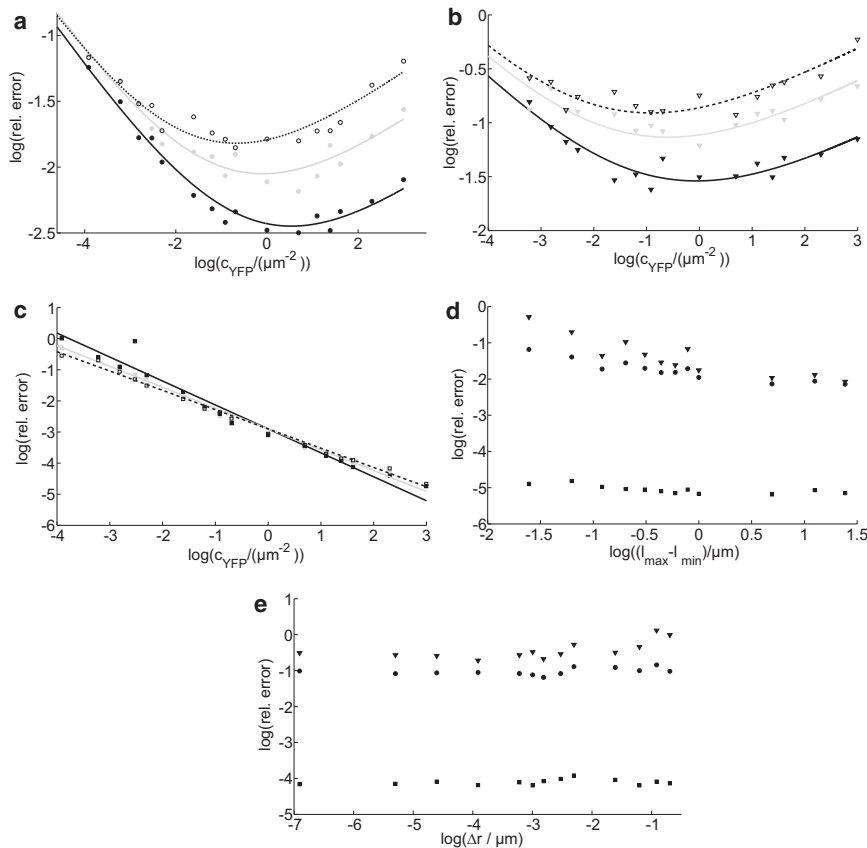


FIGURE 4 (a) Dependence of the relative error of α on the center of the fit interval $l_{center} = (l_{max} - l_{min})/2$. The legend is the same as in Fig. 3 a, where $l_{center} = 0.925 \mu\text{m}$ (solid symbols), $l_{center} = 1.175 \mu\text{m}$ (shaded symbols), and $l_{center} = 1.375 \mu\text{m}$ (open symbols). The relative error of α was fitted with the model $A \cdot (c_{YFP}/\mu\text{m}^{-2})^{-0.5} + B \cdot (c_{YFP}/\mu\text{m}^{-2})^{0.25}$. $A = 0.04$, $B = 0.05$ (solid line), $A = 0.04$, $B = 0.13$ (dashed line). That resulted in minima at $1.9 \mu\text{m}^{-2}$, $0.9 \mu\text{m}^{-2}$, and $0.5 \mu\text{m}^{-2}$, respectively. $M = 10$, $\alpha = 0.5$, and $\sigma = 0.05 \mu\text{m}$. (b) Dependence of the relative error of σ on the center of the fit interval $l_{center} = (l_{max} - l_{min})/2$. The legend is the same as in Fig. 3 a, where $l_{center} = 0.925 \mu\text{m}$ (solid symbols), $l_{center} = 1.175 \mu\text{m}$ (shaded symbols), and $l_{center} = 1.375 \mu\text{m}$ (open symbols). The relative error of σ is fitted with the model $A \cdot (c_{YFP}/\mu\text{m}^{-2})^{-0.5} + B \cdot (c_{YFP}/\mu\text{m}^{-2})^{0.25}$. $A = 0.07$, $B = 0.15$ (solid line), $A = 0.08$, $B = 0.25$ (shaded line), and $A = 0.09$, $B = 0.34$ (dashed line). That resulted in minima at $0.9 \mu\text{m}^{-2}$, $0.6 \mu\text{m}^{-2}$, and $0.4 \mu\text{m}^{-2}$, respectively. $M = 10$, $\alpha = 0.5$, and $\sigma = 0.05 \mu\text{m}$. (c) Dependence of the relative error of c_{CFP} on the center of the fit interval $l_{center} = (l_{max} - l_{min})/2$. The legend is the same as in Fig. 3 a, where $l_{center} = 0.925 \mu\text{m}$ (solid symbols), $l_{center} = 1.175 \mu\text{m}$ (shaded symbols), and $l_{center} = 1.375 \mu\text{m}$ (open symbols). The relative error of σ was fitted with the straight line (in the logarithmic plot). The slope is -0.77 (solid line), -0.67 (shaded line), and -0.62 (dashed line). $M = 10$, $\alpha = 0.5$, and $\sigma = 0.05 \mu\text{m}$. (d) Dependence of the relative errors on the length of the fit interval $(l_{max} - l_{min})$. The legend is the same as in Fig. 3 a. $M = 50$, $\alpha = 0.5$, $\sigma = 0.15 \mu\text{m}$, and $c_{YFP} = 1 \mu\text{m}^{-2}$. (e) Dependence of the relative errors on the step size Δl (Fig. 2). The legend is the same as in Fig. 3 a. $M = 50$, $\alpha = 0.5$, $\sigma = 0.15 \mu\text{m}$, and $c = 1 \mu\text{m}^{-2}$.

of fluorescent beads. The used beads were either detectable in only one color channel or both. For example, a 1:1 mixture of these two types of beads corresponds to a correlation fraction α of 0.5. Fig. 5 summarizes the results of our control experiments. As evident from Fig. 5 d PICCS faithfully retrieved the correlation fractions expected from the used bead ratios.

Dpp transport in wing disks of fruit fly larvae

Fig. 6 shows an example for an experimentally determined correlation function. A wing imaginal disk of a fruit fly larva expressing Dpp-YFP and Rab5-CFP was imaged. Rab5 is a marker for early endosomes (18). In total, 28 z stacks in both channels were taken. The endosome positions for each image in a z stack were projected into one plane resulting in 28 YFP-CFP image pairs. Fig. 6, a and b, shows the first image stack for the YFP and CFP channel. The correlation function is shown in Fig. 6 c and the cumulative probability function $P_{cum}(l)$ (Eq. 5) is shown in Fig. 6 d.

The density of CFP signals c_{CFP} and the correlation fraction α were determined by fitting a straight line to the linear part of $C_{cum}(l)$ plotted against l^2 (Fig. 6 c). The slope of this line gives $\pi \cdot c_{CFP}$ while the offset is equal to α . After subtraction of the linear contribution and division by α , $P_{cum}(l)$ remains.

In the experiments presented here, the signal intensity varied between signals and because the positional accuracy depends on the signal intensity, there is no well-defined overall positional accuracy. This variation in intensity results from variations of Dpp-YFP and Rab5-CFP content in endosomes. Furthermore, endosomes are extended objects and hence not necessarily diffraction-limited, which also influences the positional accuracy. Therefore the function given in Eq. 5, which depends on two effective correlation lengths (σ_1 and σ_2), was needed to describe the observed data. Adding more effective correlation lengths did not improve the fit significantly.

In Fig. 6, we show for one wing imaginal disk that the correlated fraction of early Rab5-CFP-labeled endosomes

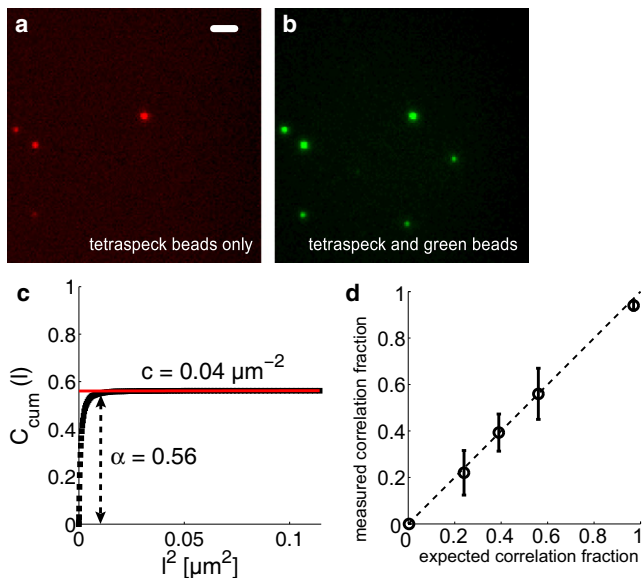


FIGURE 5 Control experiment with fluorescent beads. (a) Image from red excitation channel showing only the tetraspeck beads. (Scale bar, $2 \mu\text{m}$.) (b) Image from the green excitation channel showing both tetraspeck and yellow-green beads. (c) Cumulative correlation function for a correlation fraction of $\alpha = 0.56$. (d) Correlation fractions determined in experiments with five different ratios of single color and dual color fluorescent beads. (Dashed line) $y = x$. Errors were determined from simulations; see Error Scaling Simulation.

in the pool of all endosomes that contained Dpp-YFP in a wing imaginal disk was $\alpha_{e,Dpp} = 46 \pm 4\%$. Correction for a nonrandom distribution of CFP signals did not change this result. Conversely, the correlated fraction of Dpp-YFP containing endosomes in the pool of all Rab5-CFP-labeled early endosomes was $59 \pm 5\%$. After correction for the nonrandom distribution of YFP signals, the latter value was finally increased to $\alpha_{Dpp,e} = 66 \pm 5\%$. Hence, two-thirds of the early endosomes contained Dpp, and approximately half of the Dpp-YFP-containing endosomes were early endosomes.

Bleaching of the fluorescent label can potentially influence the results. If one of the two fluorescent labels bleaches more quickly than the other, signals are lost and the correlation fraction will decrease over acquisition time. To confirm that the number of early endosomes (CFP signal) and Dpp-containing endosomes (YFP signal) stayed constant, we measured the total number of detected endosomes per image stack (Fig. 7). On average, we detected 17 early endosomes in a field of view (one early endosome per cell on average) and the number of observed early endosomes was constant around this value. The average number of Dpp-containing endosomes found was 1.5 per cell. Fluctuations in the number of detected endosomes were caused by movement of endosomes in and out of the image volume or by endosomes that were moving too close together to be detected individually. The latter effect is corrected for in the PICCS-algorithm.

DISCUSSION

In summary, we have developed PICCS, a method to robustly quantify the fraction of correlated signals in two-color single-object or single-molecule microscopy experiments. We have derived the functional form of the cumulative correlation function and suggested a correction for nonhomogeneous distributions of signals. Control experiments with known ratios of single and dual color fluorescent beads proved that PICCS faithfully retrieves expected correlation fractions. We performed extensive simulations to obtain the dependence of the error of the method on experimental and fitting parameters. The reported error scaling will help experimenters to get exact results with minimal uncertainties.

To address whether PICCS can be applied to biological questions, we applied the method to the transport of Dpp in wing disks of fly larvae. Until now, experimental studies of that system have only been able to provide coarse-grained information, neglecting the discreteness of single cells. Recently it was shown (20) that a steady-state monoexponential gradient of Dpp concentration is formed in the target tissue. Although the latter study quantitatively described the gradient on the level of the whole tissue, it provides insufficient insight into the (sub)cellular mechanisms that underlie Dpp transport. Other experiments further suggest that Dpp is spread by three different mechanisms: diffusion in the extracellular matrix (21); receptor-mediated diffusion (22); and intracellular transport (15) (i.e., a molecule undergoes multiple rounds of endocytosis and subsequent recycling into the extracellular matrix (23)). The extracellular diffusion and receptor-mediated transport govern short-range spreading, whereas intracellular transport is essential for long-range spreading of Dpp in tissue (24).

To obtain a more detailed description of Dpp transport and to ultimately determine the contribution of each mechanism to the overall Dpp transport, these mechanisms need to be studied more extensively. Here we focused on the intracellular transport of Dpp. Because processes in this transport pathway are subcellular and involve single particles, it is necessary to use a technique such as single-particle microscopy, which can detect these individual particles with high accuracy. Three types of endosomes are involved in intracellular Dpp transport: early, late, and recycling endosomes. Measuring what fraction of early endosomes contained Dpp and vice versa in wing imaginal disks is the first step in elucidating the intracellular transport pathway of Dpp. We found that roughly two-thirds of all early endosomes contained Dpp and about half of the Dpp containing endosomes were early endosomes.

This system presented several experimental challenges which could successfully be tackled by PICCS. We found that PICCS is able to correct for a nonrandom distribution of endosomes in the wing imaginal disk. Furthermore, because the columnar cells in the wing imaginal disk have

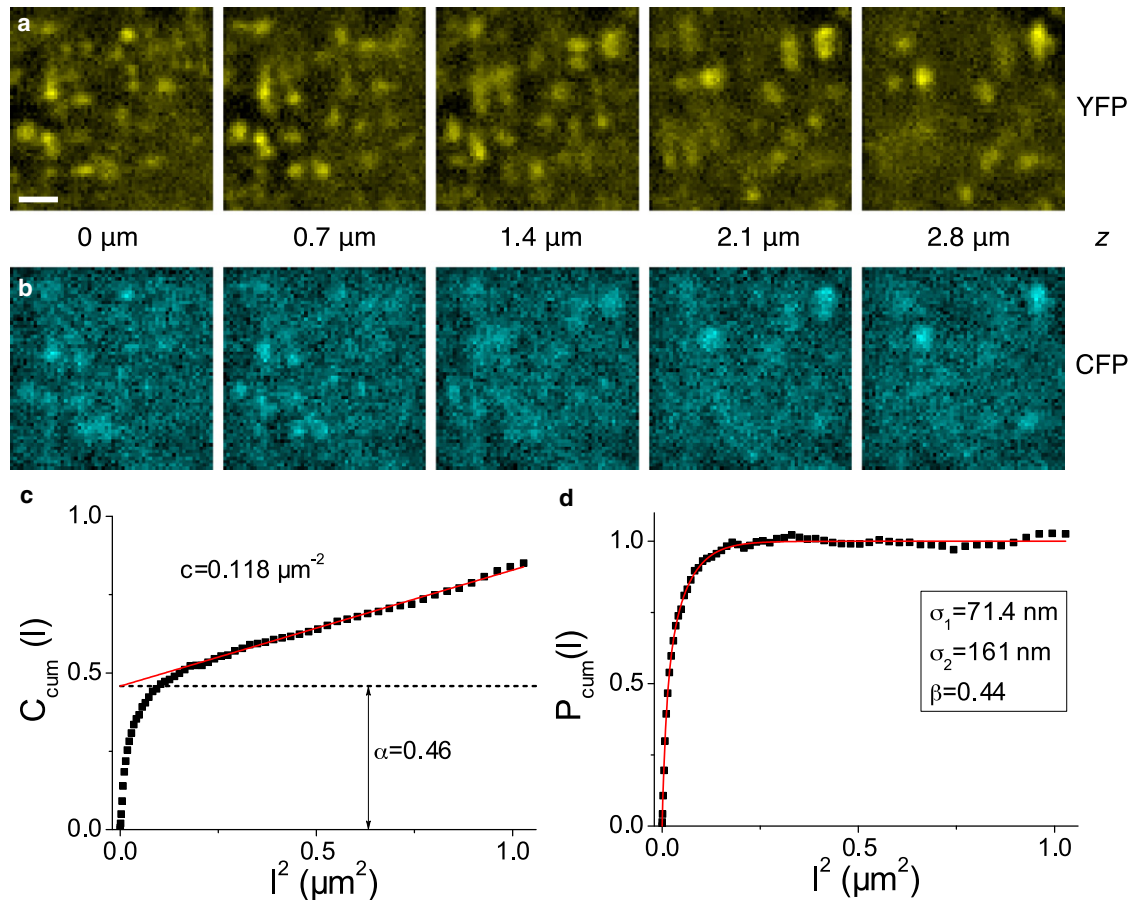


FIGURE 6 Correlation fraction, signal density, and correlation length determined from experimental data. A wing imaginal disk was imaged for 300 s using an alternating excitation method (described in Materials and Methods). Each image stack consists of five image planes ($10 \times 10 \mu\text{m}$) separated by $0.7 \mu\text{m}$ in axial direction. Background of low spatial frequency was eliminated by applying a high-pass filter. (a) Raw image stack from the Dpp-YFP channel (scale bar = $2 \mu\text{m}$). (b) Raw image stack from the Rab5-CFP channel. (c) Correlation function $C_{\text{cum}}(l)$ obtained by PICCS. Fitting of the linear part yielded a Dpp-YFP density of $c = 0.12 \pm 0.02$ endosomes $\cdot \mu\text{m}^{-2}$ (solid line) and a correlation fraction of $\alpha_{\text{e,Dpp}} = 0.46 \pm 0.04$ (offset of the fitted line). (d) $P_{\text{cum}}(l)$ which resulted from subtraction of the linear contribution from $C_{\text{cum}}(l)$ and division by $\alpha_{\text{e,Dpp}}$. The correlation lengths σ_1 , σ_2 and the fraction σ were determined by fitting Eq. 5 which gave $\sigma_1 = 71 \pm 17$ nm, $\sigma_2 = 161 \pm 34$ nm, and $\sigma = 0.44 \pm 0.17$, respectively. All errors were determined from simulations; see Error Scaling Simulation.

a length of $\sim 30 \mu\text{m}$ in axial direction and most endosomes are found in an apical layer of $\sim 5 \mu\text{m}$, the presence of out-of-focus fluorescence cannot be avoided. However, because the positions of individual particles were used, this unwanted fluorescence did not influence the PICCS results. Concerning this particular application, PICCS also holds several advantages over biochemical approaches such as endosome fractionation. Although endosome fractionation has been successfully performed on culture cells (25,26), attempts to perform endosomal fractionation in developing epithelial *Drosophila* wing cells have not been successful so far. Furthermore, endosomal fractionation would give only information on the level of the whole tissue, whereas with PICCS the differences in cargo at different positions with respect to the spatial profile of the gradient can be studied.

In the application presented above, PICCS was used to correlate two different kinds of particles at the same point

in time. By introducing a time lag, PICCS can also retrieve temporal changes correlation fraction and length, in analogy to ICCS experiments (6). Because single-particle positions can be measured with high temporal resolution, the correlation dynamics could be retrieved on timescales down to a few milliseconds. Due to the high positional accuracy of single-particle data, PICCS is not limited by diffraction, and the correlation length can therefore be determined with nanometer accuracy.

So far PICCS has been used to cross-correlate data from two channels which were separated using their different colors. The method, however, is equally applicable to any other molecular parameter that allows distinction of two species like fluorescence signal level, fluorescence lifetime, or polarization. Therefore, we believe that PICCS will be valuable not only for the study of morphogen transport but also for a broad class of biological problems involving several interaction partners.

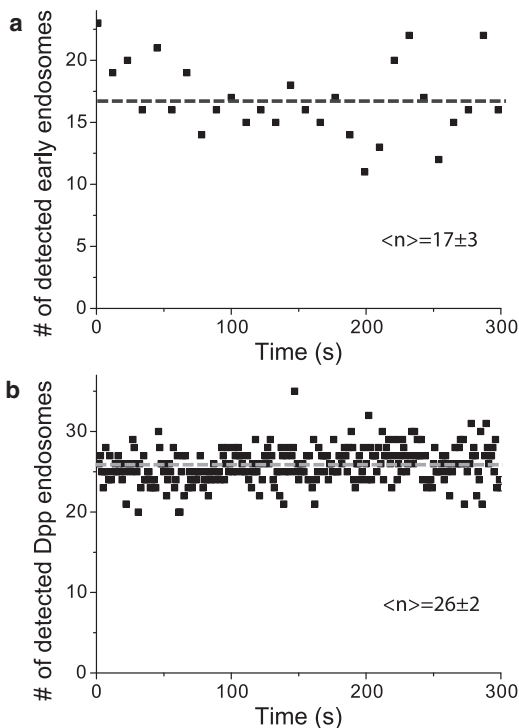


FIGURE 7 Number of detected endosomes per image stack for (a) early endosomes and (b) Dpp-containing endosomes. The number of endosomes (signals) in both channels stayed approximately constant. The average number of endosomes and the standard deviation are indicated for both cases.

SUPPORTING MATERIAL

Six figures are available at [http://www.biophysj.org/biophysj/supplemental/S0006-3495\(11\)00184-6](http://www.biophysj.org/biophysj/supplemental/S0006-3495(11)00184-6).

The authors thank Ani Kicheva and Ortrud Wartlick for discussions and for support in the genetic experiments performed in this work.

This work was supported by funds from the Human Frontiers Science Program (grant No. RGP66/2004 to L.H., M.G.-G., and T.S.), and the Dutch CYTRON consortium sponsored by the Ministry of Economic Affairs (to L.H. and T.S.). This work is part of the research program of the Stichting voor Fundamenteel Onderzoek der Materie (FOM), which is financially supported by the Nederlandse Organisatie voor Wetenschappelijk Onderzoek within the program on Material Properties of Biological Assemblies (grant No. FOM-L1707M to S.S. and T.S.). M.G.-G. was also supported by European Research Council Advanced Investigator (SARA), SystemsX (lipidsX), National Centers of Competence in Research (Chemical Biology, Swiss National Science Foundation), and R'Equip (Swiss National Science Foundation) grants.

REFERENCES

- Enderle, T., T. Ha, ..., S. Weiss. 1997. Membrane specific mapping and colocalization of malarial and host skeletal proteins in the *Plasmodium falciparum* infected erythrocyte by dual-color near-field scanning optical microscopy. *Proc. Natl. Acad. Sci. USA*. 94:520–525.
- Schütz, G. J., W. Trabesinger, and T. Schmidt. 1998. Direct observation of ligand colocalization on individual receptor molecules. *Biophys. J.* 74:2223–2226.
- Trabesinger, W., B. Hecht, ..., T. Schmidt. 2001. Statistical analysis of single-molecule colocalization assays. *Anal. Chem.* 73:1100–1105.
- Semrau, S., and T. Schmidt. 2007. Particle image correlation spectroscopy (PICS): retrieving nanometer-scale correlations from high-density single-molecule position data. *Biophys. J.* 92:613–621.
- Schwille, P., F. J. Meyer-Almes, and R. Rigler. 1997. Dual-color fluorescence cross-correlation spectroscopy for multicomponent diffusional analysis in solution. *Biophys. J.* 72:1878–1886.
- Comeau, J., S. Costantino, and P. Wiseman. 2006. Robust single-molecule approach for counting autofluorescent molecules. *Biophys. J.* 91:4611–4622.
- Comeau, J. W., D. L. Kolin, and P. W. Wiseman. 2008. Accurate measurements of protein interactions in cells via improved spatial image cross-correlation spectroscopy. *Mol. Biosyst.* 4:672–685.
- Digman, M. A., P. W. Wiseman, ..., E. Gratton. 2009. Detecting protein complexes in living cells from laser scanning confocal image sequences by the cross correlation raster image spectroscopy method. *Biophys. J.* 96:707–716.
- Digman, M. A., P. W. Wiseman, ..., E. Gratton. 2009. Stoichiometry of molecular complexes at adhesions in living cells. *Proc. Natl. Acad. Sci. USA*. 106:2170–2175.
- Basler, K., and G. Struhl. 1994. Compartment boundaries and the control of *Drosophila* limb pattern by hedgehog protein. *Nature*. 368:208–214.
- Bobroff, N. 1986. Position measurement with a resolution and noise-limited instrument. *Rev. Sci. Instrum.* 57:1152–1157.
- Schmidt, T., G. J. Schütz, ..., H. Schindler. 1996. Imaging of single molecule diffusion. *Proc. Natl. Acad. Sci. USA*. 93:2926–2929.
- Ober, R. J., S. Ram, and E. S. Ward. 2004. Localization accuracy in single-molecule microscopy. *Biophys. J.* 86:1185–1200.
- Martin, D. S., M. B. Forstner, and J. A. Käs. 2002. Apparent subdiffusion inherent to single particle tracking. *Biophys. J.* 83:2109–2117.
- Entchev, E. V., A. Schwabedissen, and M. González-Gaitán. 2000. Gradient formation of the TGF- β homolog Dpp. *Cell*. 103:981–991.
- Nagai, T., K. Iyata, ..., A. Miyawaki. 2002. A variant of yellow fluorescent protein with fast and efficient maturation for cell-biological applications. *Nat. Biotechnol.* 20:87–90.
- Marois, E., A. Mahmoud, and S. Eaton. 2006. The endocytic pathway and formation of the Wingless morphogen gradient. *Development*. 133:307–317.
- Sönnichsen, B., S. De Renzis, ..., M. Zerial. 2000. Distinct membrane domains on endosomes in the recycling pathway visualized by multi-color imaging of Rab4, Rab5, and Rab11. *J. Cell Biol.* 149:901–914.
- Holtzer, L., T. Meckel, and T. Schmidt. 2007. Nanometric three-dimensional tracking of individual quantum dots in cells. *Appl. Phys. Lett.* 90:053902.
- Kicheva, A., P. Pantazis, ..., M. González-Gaitán. 2007. Kinetics of morphogen gradient formation. *Science*. 315:521–525.
- Crick, F. 1970. Diffusion in embryogenesis. *Nature*. 225:420–422.
- Kerszberg, M., and L. Wolpert. 1998. Mechanisms for positional signaling by morphogen transport: a theoretical study. *J. Theor. Biol.* 191:103–114.
- González-Gaitán, M. 2003. Signal dispersal and transduction through the endocytic pathway. *Nat. Rev. Mol. Cell Biol.* 4:213–224.
- Kruse, K., P. Pantazis, ..., M. González-Gaitán. 2004. Dpp gradient formation by dynamin-dependent endocytosis: receptor trafficking and the diffusion model. *Development*. 131:4843–4856.
- Goebeler, V., M. Poeter, ..., U. Rescher. 2008. Annexin A8 regulates late endosome organization and function. *Mol. Biol. Cell*. 19:5267–5278.
- Morel, E., and J. Gruenberg. 2009. Annexin A2 binding to endosomes and functions in endosomal transport are regulated by tyrosine 23 phosphorylation. *J. Biol. Chem.* 284:1604–1611.